Rain Motion Vectors Analysis From the Radar Network in Italy

Mario Montopoli, Clizia Annella, Luca Baldini, *Senior Member, IEEE*, Elisa Adirosi, Vincenzo Capozzi, and Gianfranco Vulpiani

***Abstract*—In-cloud motion vector retrieval is of great interest in several atmospheric science research fields. Short time extrapolation of radar data (precipitation nowcasting), assimilation into numerical weather prediction models, study of atmospheric circulation, as well as reference scenarios for future satellite missions, are glaring example where the knowledge of in-cloud motion vectors can play a relevant role. In this work, a dataset of nearly one-year and half of measurements collected by ground-based weather radars over the Italian peninsula, is used to perform the reconstruction of horizontal in-cloud rain motion vectors (RMVs) using both optical flow-based solutions from literature and an innovative extension of the multiple Doppler solution that make use of mosaicked Doppler radar data. The outcomes of the techniques implemented are analyzed in terms of reference Doppler measurements, reanalysis wind fields from ERA5 and evaluating the impact of the RMVs in a semilagrangian precipitation nowcasting framework. To the author knowledge, this is the first attempt in quantitatively evaluating RMVs. Results show that the use of Doppler information enhances the dynamic range of the retrieved RMV intensity with respect to optical flow-based solutions giving a better agreement with the ERA5 too. In terms of precipitation nowcasting, the use of Doppler-driven RMV does not give significant improvements due to gradients shown by RMV intensity when constrained with the measured Doppler.**

***Index Terms*—Doppler weather radar, in-cloud motion vectors, precipitation, wind fields.**

I. Introduction

SEVERE winds can cause widespread harms to infrastructures, such as buildings, transport, and energy networks, as well as to natural ecosystems, e.g., forests, coastal areas prone to erosion etc. Several international reports [e.g., European[1]] documented as severe winds are responsible of 5 billion Euros of economic losses in the EU and U.K. In clear sky or thin clouds, wind information can be inferred locally using radiosoundings (RAOBS), wind lidars, high frequency radars, and wind profilers from ground and space. In this respect, the European Space Agency (ESA) Aeolus mission [1], that flew the first space-based Doppler wind lidar from 22 August 2018 to 30 April 2023, demonstrated the capability for global observations of 35° off-nadir wind profiles. These measurements demonstrated to be of good enough quality to improve weather forecasting [2], [3], [4]. However, in cloudy conditions, lidar-based techniques are impractical or unsuccessful because clouds and rain shafts tend to blind the sensor's penetration capability through clouds. In such scenarios, as early as 1968, [5], [6], infrared and visible sensors aboard geostationary satellites offered the opportunity to track air masses capturing cloud-tops or water vapor movements in successive satellite images on a continental scale to extract atmospheric motion vectors (AMVs) and then infer horizontal winds [7]. AMVs are important information, especially in less-covered areas (e.g., oceans) for the quantitative description of atmospheric circulations, as well as for improving the weather forecasts providing wind field proxies for assimilation purposes [8], [9]. Over ocean, radar scatterometers add a further observational opportunity allowing for the near surface wind estimation exploiting the interaction of winds and ocean weaves [10].

Nevertheless, none of the aforementioned techniques provide information into clouds systems. Retrievals within the clouds are typically performed in the microwave region of the EM spectrum, at centimeter and millimeter wavelengths, due to their capability to penetrate clouds up to some extent, depending by the used wavelength. Nowadays, however, such approaches do not provide the in-cloud dynamic. In the near future, the W-band Cloud Profiling Radar onboard ESA-JAXA EarthCARE platform [11], planned to be launched in the mid 2024, will be able to measure vertical in-cloud Doppler profiles but, due to the nadir pointing, it will not be able to obtain the information about the horizontal cloud movement. The INvestigation of Convective UpdraftS mission is a NASA Earth Ventures Mission [12], which is planned to be launched in 2026 with an expected lifetime of two years, will aim to capture vertical motions of convective

Manuscript received 6 January 2024; revised 1 March 2024 and 23 April 2024; accepted 28 May 2024. Date of publication 5 June 2024; date of current version 1 July 2024. *(Corresponding author: Mario Montopoli.)*

Mario Montopoli is with the National Research Council of Italy, Institute of Atmospheric Science and Climate (CNR-ISAC), 124228 Rome, Italy, and also with the Center of Excellence for Telesensing of Environment and Model Prediction of Severe events, Università Dell'Aquila, L'Aquila, 67100 L'Aquila, Italy (e-mail: mario.montopoli@cnr.it).

Clizia Annella is with the Center of Excellence for Telesensing of Environment and Model Prediction of Severe events, Università Dell'Aquila, 67100 L'Aquila, Italy (e-mail: clizia.annella@univaq.it).

Luca Baldini and Elisa Adirosi are with the National Research Council of Italy, Institute of Atmospheric Science and Climate (CNR-ISAC), 124228 Rome, Italy (e-mail: luca.baldini@cnr.it; elisa.adirosi@cnr.it).

Vincenzo Capozzi is with the Dipartimento di Scienze e Tecnologie, Università degli studi di Napoli "Parthenope," CAP80143 Naples, Italy, and also with the National Research Council of Italy, Institute of Atmospheric Science and Climate (CNR-ISAC), 124228 Rome, Italy (e-mail: vincenzo.capozzi@uniparthenope.it).

Gianfranco Vulpiani is with the Civil Protection Department, Presidency of the Council of Ministers, 00189 Rome, Italy (e-mail: gianfranco.vulpiani@protezionecivile.it).

Digital Object Identifier 10.1109/JSTARS.2024.3410031

[1] [Online]. Available: European commission report

systems. It proposes a novel time-differencing approach among observations of three satellite borne Ka-band radars flying in tandem (30, 90, and 120 s apart) to estimate vertical fluxes that characterize the rapid evolution of convective clouds across the tropics. Finally WIVERN [13], an ESA Earth explorer 11 mission, currently running the phase A, has the unique opportunity, thanks to its W-band radar with slanted conical scan, to obtain horizontal in-cloud winds mainly in stratiform precipitation regimes. Thus, at the current state of the art, only weather radars give the opportunity to acquire in-cloud rain motion vector (RMV) information on large domains over land, at kilometer resolution and minute time sampling. Weather radars use rain drops as tracer for rain field motion retrievals. This can be achieved in two distinct ways: advection- and Doppler-based techniques. The former exploits a time sequence of past radar images to extract the motion field of precipitation systems, similarly to what is done in AMVs. In this respect, several techniques were developed so far. The most relevant can be grouped as follows.

1) Methods based on the maximization of cross-correlation over subgrids in two successive radar images [14], [15], [16].
2) The variational approaches, e.g., the Continuity of Tracking Radar Echos by Correlation [17], which aims to regularize the solution of more classical cross-correlation methods by minimizing a cost function that include the continuity equation of the motion field; or the variational echo tracking (VET) [18], [19] that implement minimization procedures of a cost function between the displaced and the reference radar image.
3) The dynamic and adaptive radar tracking of storms (DARTS) [20], which uses a spectral approach to solve the optical flow equation.
4) The Lucas and Kanade (LK) approach [21] that solves the optical flow equation by building a set of linear equations from neighbor pixels in a visited subregion and applies the least square minimization to solve the equation system.

The Doppler-based approaches rely on the direct and instantaneous measurement of hydrometeors movement with respect to the radial direction from the radar position, exploiting the Doppler effect. Since the Doppler gives only the line-of-sight component of the unobserved true rain motion field, coincident Doppler measurements from at least two different radar sites (i.e., multi-Doppler synthesis) are typically needed to convert the Doppler information into zonal (West to East) and meridional (South to North) rain motion components. This makes the multi-Doppler technique applicable only in the overlapping areas of the involved radars. In this work, an extension of the multi-Doppler technique, named Doppler cell (DC), is proposed and tested together with advection-based methodologies: VET, DARTS, and LK. The DC procedure adopted in this study is based on what initially reported in Song et al.'s [22] work and further elaborated in [23], [24], and [25]. However, the work in Song et al.'s [22] was conceived for a satellite-borne view geometry while the achievements in [23], [24], and [25] allow the 3-D retrieval of the wind fields but require the overlapping coverage from at least two radars. In addition, these procedures work starting from radar data volumes that are not always everywhere available. Contrarily, the DC method works with already sampled Cartesian data and does not strictly require overlapping areas among radar coverage making it a more flexible choice. The performance of the RMV techniques tested in this work is evaluated using the following.

1) Doppler data (for VET, DART, and LK only).
2) Performing direct comparisons between RMV components with those from the European Centre for Medium-Range Weather Forecasts (ECMWF) ERA5 reanalysis wind fields [26].
3) Evaluating the performance of a fixed precipitation nowcasting extrapolation scheme as a function of the various input RMV tested.

The dataset employed in the analysis is made of 17 months from the Italian national radar composites in terms of Constant Amplitude Plan Position Indicators (CAPPIs) at 2 and 4 km of altitude for both the reflectivity factor (Z) and Doppler velocity (V). To the best of our knowledge, the adopted Doppler RMV methodology as well as the way to characterize the estimation error has elements of novelty since Doppler rain motion field reconstruction is little or not at all used in radar meteorology from an operational stand point. As it will be demonstrated in this manuscript, the procedure to derive RMV from Doppler radar measurements is flexible and computationally fast enough to be implemented operationally on a national wide scale. In the near future, this could open the opportunity to populate new databases of precipitation system dynamics with applications in local wind climatology and market analysis in the insurance sector.

The rest of this article is organized as follows. Section II describes the reference ERA5 wind data, Section III-A describes the weather radar data processing and collected dataset as well as the expected Doppler performance. Section IV describes the considered methodologies for motion vectors estimation, whereas, Section V discusses the results in terms of the error characterization. Finally, Section VI concludes this article.

II. ERA5 Wind Data

The ECMWF ERA5 reanalysis [26] is the fifth generation ECMWF reanalysis that describes the state of atmosphere at global scale from 1940 onwards. Reanalysis combines model data with observations providing a globally complete seamless and consistent regular-grid dataset. The temporal resolution is of 1 h, whereas the horizontal one is $0.25^\circ \times 0.25^\circ$ (approximately 31 km) with 37 pressure levels from 1 to 1000 hPa.

In this study, ERA5 wind products at 800 and 650 hPa are used as reference scenarios for comparison with radar Doppler observations and RMV retrievals. In this respect, ERA5, due to its model based-nature, can suffer from lack of representativeness of single episodes although it certainly is the easiest starting point due to data readiness and availability. Indeed, in some circumstances, ERA5 could be spatially and temporally misaligned with respect to the radar fields to be compared but it is reasonable to expect that considering a long time series, the two information have to converge on average (i.e., in terms

of small bias). However, ERA5 wind's reliability was studied in previous studies although none of them have specifically interested Italy. In Taszarek et al. [27], their table 3, produced an error statistic of ERA5 comparison with RAOBS over Europe and North America in the period 1980–2018, in terms of 850-hPa wind speed (which is the variable considered in our study) and found a bias (ERA5-RAOBS) of –0.28 ms^{-1} (which reduces to =–0.2 ms^{-1} for zonal and meriodional winds assuming the bias equally distributed between these two components) and a root mean square error of 1.91 ms^{-1}. The authors in [27] and [28] evaluated ERA5 850-hPa zonal wind (meridional wind) for the central Taklimakan Desert in China from June 25 to July 3, 2015 and the entire July 2016. They found a bias of 0.0 (0.1) ms^{-1} and root mean square error of 3.5 (4.0) ms^{-1}.These results indicates a small tendency of ERA5 to underestimate RAOBS up to 0.2 ms^{-1} in the meridional and zonal components. However, in absence of any specific indication of ERA5 biases over Italy, in the following, we preferred to leave the ERA5 wind product unmodified.

As a last consideration, it is worth mentioning that other options, rather than ERA5, were evaluated before choosing ERA5. However, those options, unfortunately, do not cover the target period covered by our radar dataset (2022–2023). The alternative reference dataset we paid attention to, are as follows.

1) MEteorological Reanalysis Italian DAtaset (MERIDA) product, [29], which proposes a 4-km dynamical downscaling of the e ERA5 for Italy, from 1986 to 2021, using the weather research and forecasting model.
2) Copernicus European Regional ReAnalysis (CERRA) [30], which is available for the European territory at 5.5 km horizontal resolution, from 1984 to 2021.

Direct use of numerical weather predition (NWP) models could be another possibility but, in this case, direct historical NWP outputs are not easily available. On top of this, the higher resolution of those models associated to the model spin-up time, makes the space–time misalignment with observation more severe than using reanalysis, and for these reasons we chose to discard this option.

III. Weather Radar Mosaic Data

A. Italian Radar Network Description

Weather radar data used in this study come from the Italian radar network which is currently composed by 20 C-band and six X-band systems. The network is managed by 13 administrations, covering most of the country. The product generation is centralized at national level by the Department of Civil Protection that currently manages seven C-band and four X-band systems, all with dual-polarization capability. The national mosaic includes several gridded products projected into $N_x \times N_y$ matrix with grid spacing of 1×1 km^2: precipitation intensity, pseudo CAPPIs of reflectivity factors (Z) at altitudes from 2 to 8 km, and those of Doppler velocity (V) at 2 and 4 km levels as well as vertical maximum intensity and warning products.

In case of V, for each grid point of the final composite, data are taken from the nearest radar acquisition contributing to the visited location. In addition, in order to correctly interpret the multiple-radar Doppler signatures, the view direction information of each radar, in terms of antenna elevation (θ) and azimuth (ϕ), are stored together with V for each grid point of the radar network domain. The distribution of θ, sampled in precipitation regimes from January 2022 to May 2023 and considering those radar grid points in CAPPI at 2 km that survive after the data screening described in Section II.C, are considered. A data quality variable (Q) [31], which takes into account identified artifacts, partial beam blocking, measurement height relative to freezing level, beam broadening with distance, and rain path attenuation, underlies each product generated. The use of Q allows the user to tune the quality of the final products performing postprocessing quality checks.

B. Dataset

The collected dataset of the radar mosaics consists of pseudo-CAPPI in the target period from 1st of January 2022 to 31st of May 2023 for both Z and V at 2 ± 0.5 and 4 ± 0.5 km, characterized by spatial and temporal resolution of 1×1 km^2 and 10 min, respectively. A fast and easy radar frame selection rule, based on the file size, is adopted to exclude from the analysis radar frames that do not include a significant amount of precipitation data. The main assumption is that in the target period, most of the radar acquisitions are essentially referred to clear air conditions. Under this assumption, the most frequently occurring value (i.e., the statistical mode) of the distribution of the radar frame file sizes can be a good indicator for quickly separating clear air conditions from rainy periods. Such selection procedure is applied to our radar dataset with a file size lower threshold of 46.8 kB (which coincides with at least 0.3% of wet pixel in each radar image) leading to the final selection of about 33 000 radar frames. However, it should be noted that the threshold criteria based on the file size, could depend by the specific data format and data compression used. Thus, a more general but relatively less fast screening approach might consider the percentage of wet grid points within each radar image. To have an overall idea of the seasonal distribution of the dataset used, the relative frequency of the radar frames that populate the various months is shown in Fig. 2, indicating that the Summer season is less represented in our data.

C. Data Processing

Although some gross artifacts are removed during the mosaicking process, a further post processing is applied to remove residual unwanted effects in the CAPPIs. In more detail, a data screening is applied excluding all the measurements that comply with the following rule:

$$\text{Exlude data if:} \quad Z < Z_{\text{th}} \text{ or } Q < Q_{\text{th}} \text{ or } |V| > V_{\text{th}} \qquad (1)$$

where the thresholds Z_{th}, Q_{th}, and V_{th} are set to 0 dBZ, 60% and 38 ms^{-1}, respectively. Such thresholds are fixed after a thorough analysis and visual inspections of know artifacts. An example of the mosaic data in terms of Z and V is shown in Fig. 3. In this figure, the grey area shows the nominal radar coverage while the dark green stains over land represent removed artifacts (e.g.,

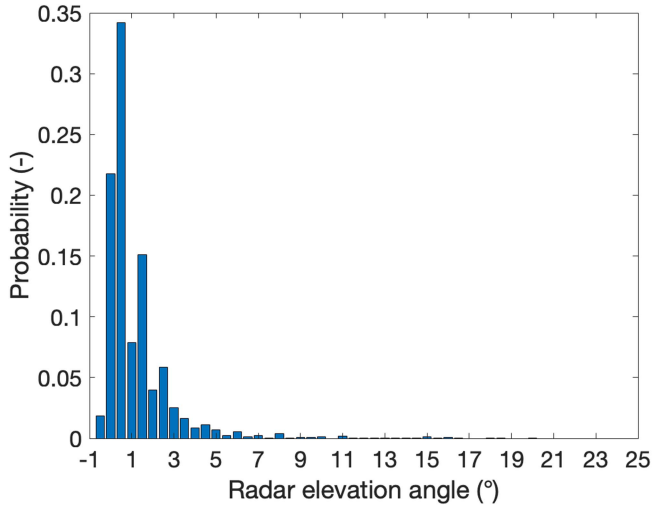

Fig. 1. Statistical distribution of the radar elevation angles, built considering all wet grid points that contribute to CAPPI-2 km product sampled from 1st of January 2022 to 31st of May 2023. Only those radar grid points that survive after the data screening described in (1), are considered.

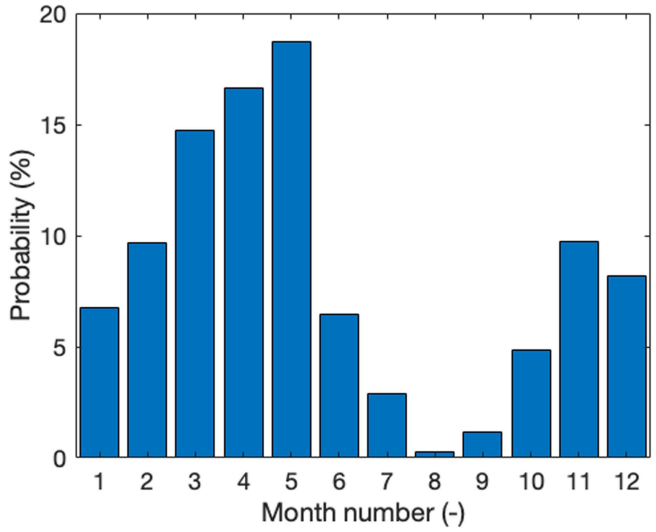

Fig. 2. Monthly distribution of the radar frames populating the selected radar dataset from 1st of January 2022 to 31st of May 2023.

clutter) after the filtering in (1). The black circles indicate the radar positions and can aid in the interpretation of the mosaicked Doppler.

D. Doppler Data Quality Test

Since one important innovation brought by this work is on the exploitation of Doppler mosaic, one aspect that needs to be evaluated before any subsequent analysis, is to check the overall radar Doppler quality. To this end, without any external reference information of in-cloud dynamic, we compared the Italian dataset, in terms of Doppler acquisitions, with hourly co-located 31-km spatial resolution ERA5 winds at 800 and 650 hPa. ERA5 fields are interpolated on the 1×1 km radar network grid using a cubic spline function and then projected on the Doppler view directions for all in-cloud rainy grid points before proceeding with the comparison. To homogenize the spatial resolutions between ERA5 and radar measurements, the latter are upscaled (i.e., averaged) on a 31×31 km.

The result of such a comparison is shown in Fig. 4 where data from all the dataset are included (panel a). The agreement of ERA5 and radar Doppler is fairly good with a bias (ERA5−Doppler) oscillating between $[-1.3, -1.4]$ ms^{-1} (see the in-plot statistics). One surprisingly aspect of this comparison is that there is not an appreciable bias difference when considering CAPPI at 2 km (blue curve) or at 4 km (red) altitudes. This can be partially due to the fact that CAPPI are built considering all data in the altitude interval of ± 0.5 km so that they are representative of a wide vertical domain. In terms of standard deviation of the difference, values larger than 5.5 ms^{-1}, are registered. In theory, data at 4 km altitude are expected to be more directly related to winds, being the particles sampled by the radar at that altitude mainly composed by ice, so that they are more efficiently transported by winds. However, this also implies that at 4 km altitude, particles react faster to wind variations too. This likely explains the additional 1 ms^{-1} standard deviation found at 4 km than at 2 km. Panel b) of Fig. 4 replicates the panel a) except that in this case only those Doppler difference having both Doppler-projected from ERA5 and that measured from the radar with the same sign (POS-only), are represented. Doing so, bias is reduced by almost half well below 1 ms^{-1} with small reduction in the standard deviation. In conclusion, although measured Doppler is a quantity sensitive to the hydrometer relative motion whereas the ERA5 is a representation of the wind (i.e., movement of air masses), both of them seem to be in a good overall agreement. In addition, since the comparison at 2 and 4 km does not show any substantial difference, henceforth 2 km-CAPPIs only are used.

IV. RMV Estimation Methodology

In this section, the algorithms used to estimate the RMVs from radar data are introduced. Three methods from literature used in this work, namely, LK [21], DARTS [20], and the VET [18], are briefly summarized in the following sections. On top of these, an additional approach, called DC, that makes use of mosaicked Doppler, is described. In our knowledge, so far, the DC solution, as formulated in the following sections, has never been tested to mosaicked ground radar data. In this work, the implementation of the algorithms used to estimate the RMVs is carried out with the default pysteps configuration available in GitHub.[2] As highlighted previously by Pulkkinen et al.'s [32] work, it is important to note that DARTS and LK require significantly less computational time than VET. In contrast, DARTS requires a longer sequence of radar images to estimate motion (for the results that follow, we used six consecutive radar frames for DARTS and two for LK and VET).

A. LK RMV

The LK approach is an image processing technique that solves the optical flow equation in a given grid point (x, y) of the radar

[2][Online]. Available: https://pysteps.github.io, last access: 24 November 2023

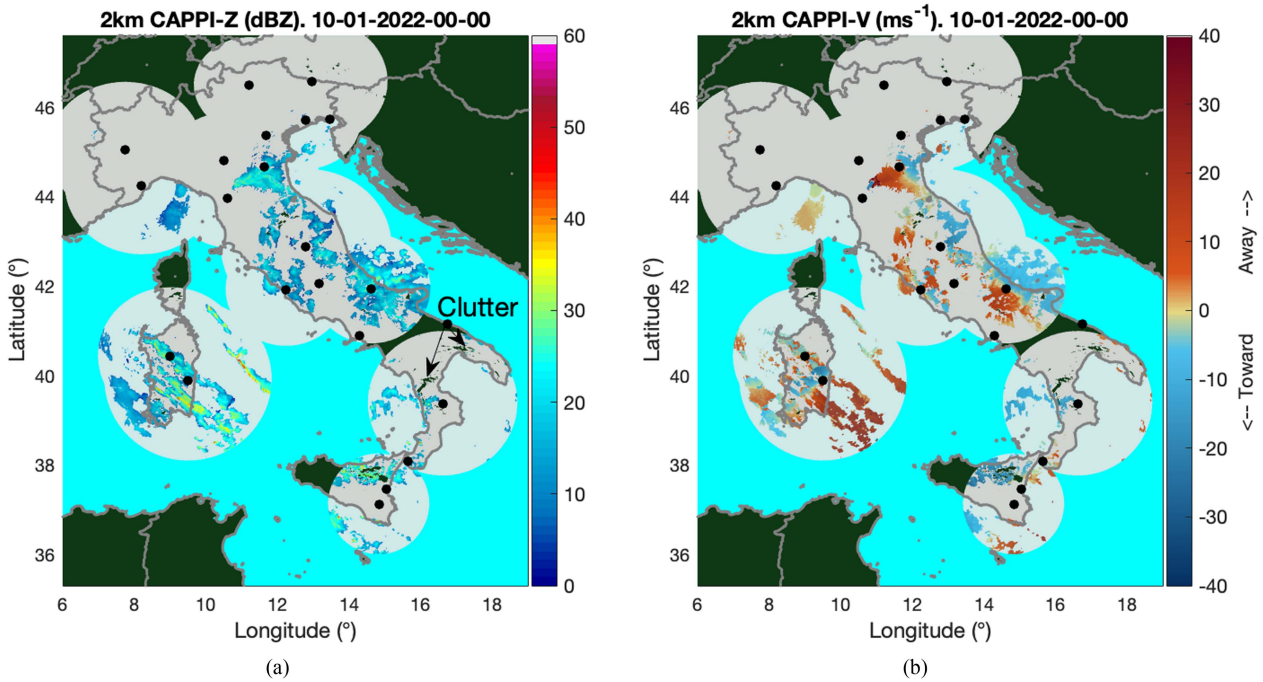

Fig. 3. Example of Italian radar Mosaic (10-01-2022, 00:00 UTC) in terms of reflectivity factor (a) and Doppler velocity (b). Black dots represent the single radar position. The gray areas represent the nominal maximum range coverage of each radar.

frame, having N_x rows and N_y columns (see Fig. 5), using information within a moving analysis window. The optical flow equation is a special case of the mass conservation law where in our case the "mass" is represented by Z and source sink terms are assumed to be zero

$$\left[\frac{\partial Z(x,y,t)}{\partial x}\right] U_x + \left[\frac{\partial Z(x,y,t)}{\partial y}\right] U_y + \left[\frac{\partial Z(x,y,t)}{\partial t}\right] = 0. \tag{2}$$

The notation $Z(x, y, t)$ indicates the reflectivity factor at position (x, y) and time t. Since (2) has two unknowns, namely, the West to East motion vector (U_x) and the South to North component (U_y), at least one further equation is needed. Note that the vertical component (W_z) is neglected in (2) since the radar elevation angles rarely exceed 20° making, in most of cases, the vertical components reasonably negligible with respect to the horizontal ones. LK solved this ill-posed problem building a linear system by replicating (2) for multiple grid points within a $N_p = n \times n$ moving window. Fig. 5 clarifies the working geometry. Thus, collecting the derivative terms $\frac{\partial Z(x,y,t)}{\partial x}$, $\frac{\partial Z(x,y,t)}{\partial y}$ for N_p grid points in a $N_p \times 2$ matrix ($\mathbf{A}$) and the terms $\frac{\partial Z(x,y,t)}{\partial t}$ in a $N_p \times 1$ vector ($\mathbf{b}$), a simple linear system $\mathbf{AU} = \mathbf{b}$ is obtained, whose solution is

$$\mathbf{U} = \mathbf{A}^{-1}\mathbf{b} \tag{3}$$

with the wind vector $\mathbf{U}$

$$\mathbf{U}(x, y, t) = [U_x(x, y, t), U_y(x, y, t)]^T. \tag{4}$$

Note that the presence of the time derivative term of Z implies the necessity to consider at least two radar frames at sequential time steps, t and $t - \Delta t$.

B. DARTS RMV

The DARTS technique [20] uses a spectral approach to solve the (2). It applies the 3-D discrete Fourier transform (DFT) to the N_t-time series of observed $N_x \times N_y$ frames of reflectivity fields, $Z(x, y, t)$. So doing, (2) can be rewritten in the spectral domain as a function of the spatial (k_x, k_y) and temporal (k_t) wave number variables. The advantage of this approach is twofold: i) in the spectral domain, the derivatives of Z with respect to x, y, and t become a standard product between k_x, k_y, k_t, and the DFT field $\tilde{Z} = Z_{\text{DFT}}(k_x, k_y, k_t)$; ii) the degree of smoothness of the estimated motion field can be easily controlled by the level of truncation of the DFT coefficients. The main drawback is that more than two time frames are needed to efficiently calculate DFT in the time domain. The (2) in the Fourier domain is then written as follows:

$$\frac{k_t \tilde{Z}}{N_t} = -\frac{(\tilde{U_x} \star k_x \tilde{Z})}{N_x^2 N_y} - \frac{(\tilde{U_y} \star k_y \tilde{Z})}{N_x N_y^2} \tag{5}$$

where the $''\tilde{}''$ hat symbol represents a DFT transformed quantity and $''\star''$ is the convolution operator. Note that (5) differs slightly from that reported in Ruzanski and Chandrasekar's [20] work because the harmonic truncation is not considered in our formulation.

Equation (5) can be reorganized in matrix form and then solved with a least-squares approach. The solution is in terms of 2-D-DFT: $\tilde{U}_x(k_x, k_y)$, $\tilde{U}_y(k_x, k_y)$. Hence, an inverse DFT is applied to obtain the final solution.

C. VET RMV

In this approach the motion field is estimated by an adaptation of the VET technique first presented by Laroche and

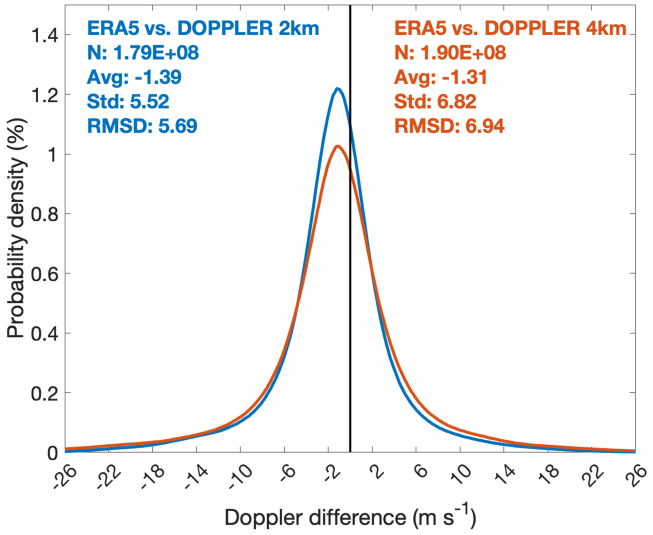

(a)

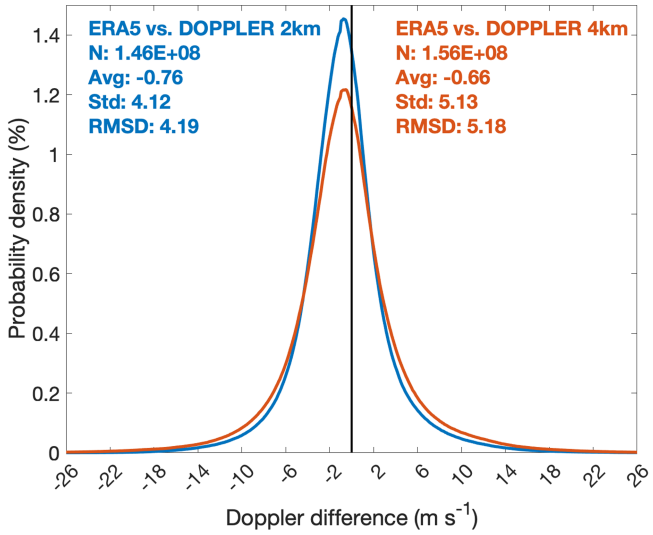

(b)

Fig. 4. Doppler difference (Doppler projected ERA5—measured Doppler) using CAPPI 2 km (blue) and 4 km (red) for all grid points in the dataset (panel a) and considering only those grid points where measured radar Doppler and that reconstructed from ERA5 have the same sign (panel b). In the panels, legend N, Avg, Std, and RMSD indicate the number of samples, the average and standard deviation difference and the RMSD, respectively.

Zawadzki [18]. This algorithm computes the displacement field ($\mathbf{U}\Delta t$) between two radar frames separated by a certain time interval Δt, namely $Z(\mathbf{s}, t)$ and $Z(\mathbf{s}, t - \Delta t)$ with $\mathbf{s} = (x, y)$, by minimizing a cost function J_{VET} consisting of two constraints as follows:

$$J_{\text{VET}}(\mathbf{U}) = J_\psi + J_V. \tag{6}$$

The second term in (6), J_ψ, represents the conservation of reflectivity constraint and it is defined as the sum of squares of the echo residuals in the spatial domain Ω and it is expressed as follows:

$$J_\psi = \int\int_\Omega \beta(\mathbf{s})[Z(\mathbf{s}, t) - Z(\mathbf{s} - \mathbf{U}\Delta t, t - \Delta t)]^2 dxdy \tag{7}$$

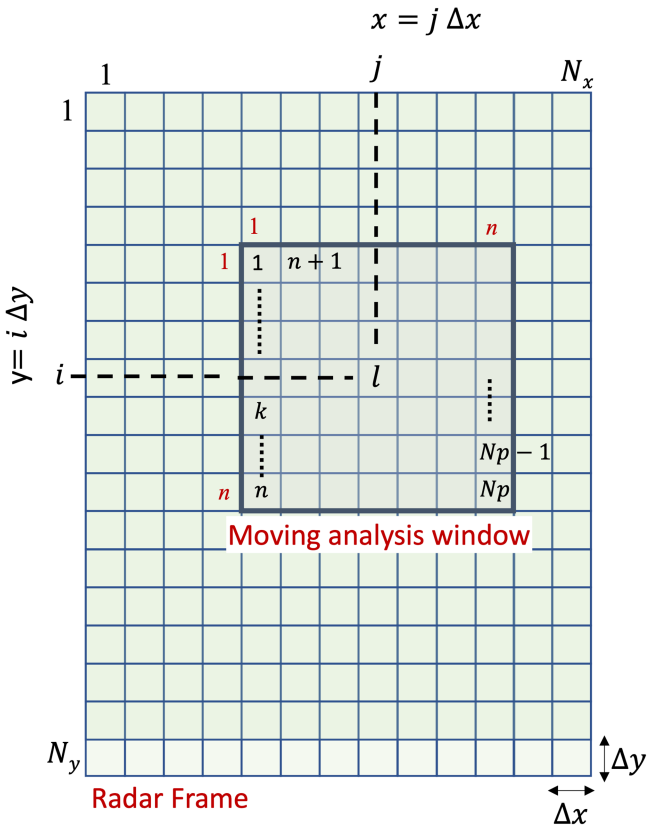

Fig. 5. Representation of the radar network grid overimposed to the analysis moving window.

where $\beta(\mathbf{s})$ denotes the weight of the reflectivity constraint that is generally related to data quality but, in most applications, is made to be a constant throughout the domain of integration. The third term of (6) is a smoothness penalty function and its equation is as follows:

$$J_V = \gamma \int\int_\Omega \left(\frac{\partial^2 U_x}{\partial x^2}\right)^2 + \left(\frac{\partial^2 U_x}{\partial y^2}\right)^2 + 2\left(\frac{\partial^2 U_x}{\partial x \partial y}\right)^2 + \left(\frac{\partial^2 U_y}{\partial x^2}\right)^2 + \left(\frac{\partial^2 U_y}{\partial y^2}\right)^2 + 2\left(\frac{\partial^2 U_y}{\partial x \partial y}\right)^2 dxdy \tag{8}$$

where γ is a constant weight. To minimize the cost function, VET uses the conjugate-gradient algorithm described by Navon and Legler [33]. In order to reduce the probability of converging toward a secondary minimum, the scaling guess procedure developed by Laroche and Zawadzki [34] is used to determine the best motion field.

D. DC RMV

The DC technique is an extension of the multiple Doppler syntheses [35] which original formulation was proposed by Song et al. [22] for a satellite view geometry. While multiple Doppler syntheses generally require two or more coincident Doppler measurements at the same location, the former exceeds such a limitation but paying the cost of a lower resolution of the final result. In addition, multiple Doppler syntheses is limited to the overlapping regions of the coverage of the involved radars only,

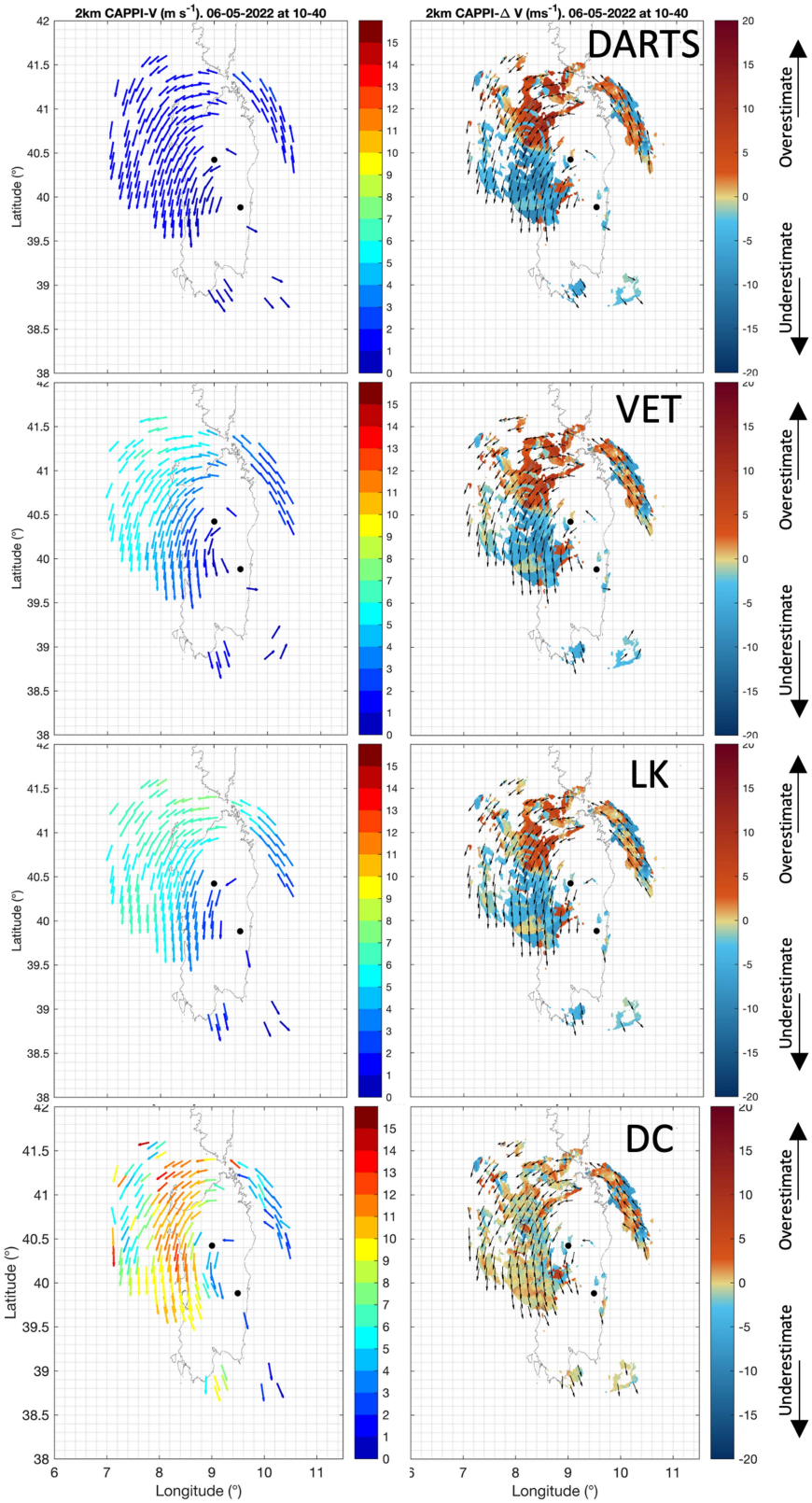

Fig. 6. Examples of RMV (left) and Doppler difference after projecting RMV into Doppler geometry (right) in terms of CAPPI-2 km for a case study occurred over the Sardinia island (Italy) on 6th May 2022 at 10:40 UTC. The black dots indicate the radar sites that are contributing to the network. RMV fields on the left panels are represented as unit vectors with the magnitude of each vector (ms^{-1}) described by respective colorbars.

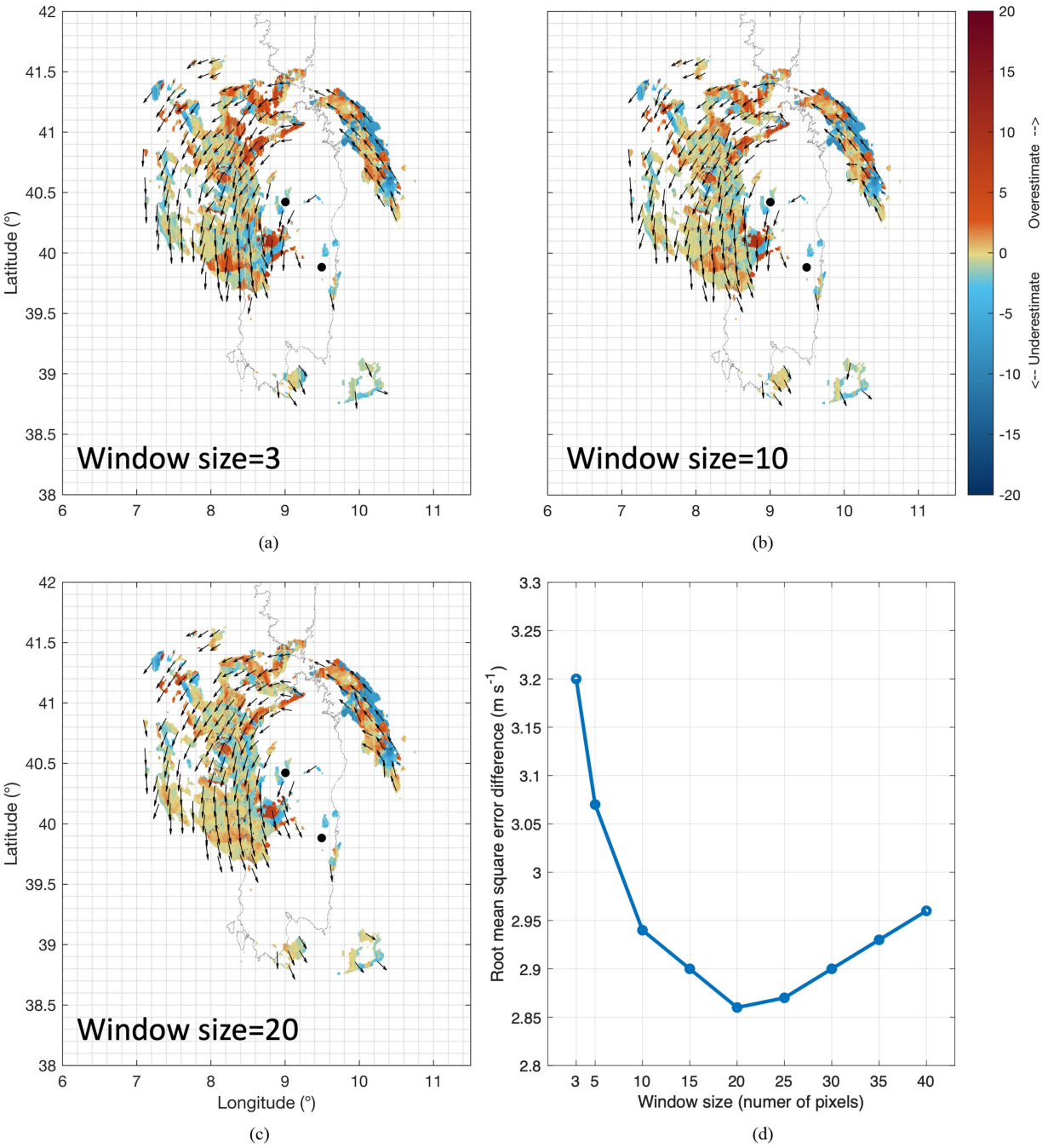

Fig. 7. Error sensitivity in terms of Doppler difference maps in (ms^{-1}) (i.e., measured radial Doppler velocity minus the reconstructed one, the latter being obtained projecting the estimated RMV onto the radial directions. Different window sizes, used in the DC method, are tested (a)–(c) for the case study on 6th May 2022. Behaviour of root mean square error of the Doppler difference as a function of several DC window sizes (d).

which is a condition that is not always easily found. Indeed, the Doppler velocity measured by a radar at the kth grid point of the radar frame at time t and referred to a generic observation line of sight, is given by

$$V_{Dk} = U_x \sin(\phi_k)\cos(\theta_k) + U_y \cos(\phi_k)\cos(\theta_k) + W_h \sin(\theta_k) \tag{9}$$

in which θ_k and ϕ_k, define the direction of observation in terms of elevation and azimuth angles, respectively, U_x, U_y, and W_h are the three unknown Cartesian component of the motion vector for the kth grid point and V_{Dk} is the resulting Doppler velocity. For brevity, in (9), we used the following notation $V_{Dk} = V_D(k)$, $\theta_k = \theta(k)$, and $\phi_k = \phi(k)$. Indeed, to facilitate the implementation of the DC method, the last term in (9), namely $W_h \sin(\theta_k)$, is neglected. This can potentially impact the estimated component U_x, U_y when trying minimizing the deviation between the measured Doppler and the imperfectly reconstructed one [i.e., assuming $W_h \sin(\theta_k) = 0$ in (9)]. However, it should be noted as in the Italian radar network, the distribution of the elevation angles used to generate CAPPI-2 km (see Fig. 1) is limited by

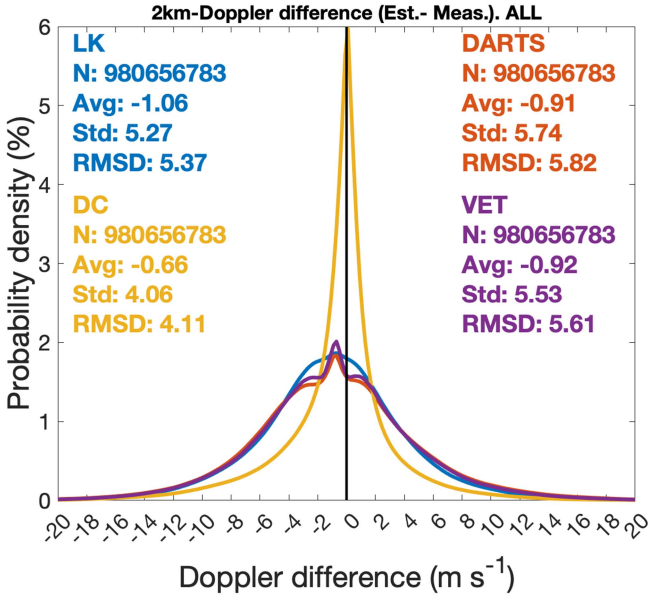

(a)

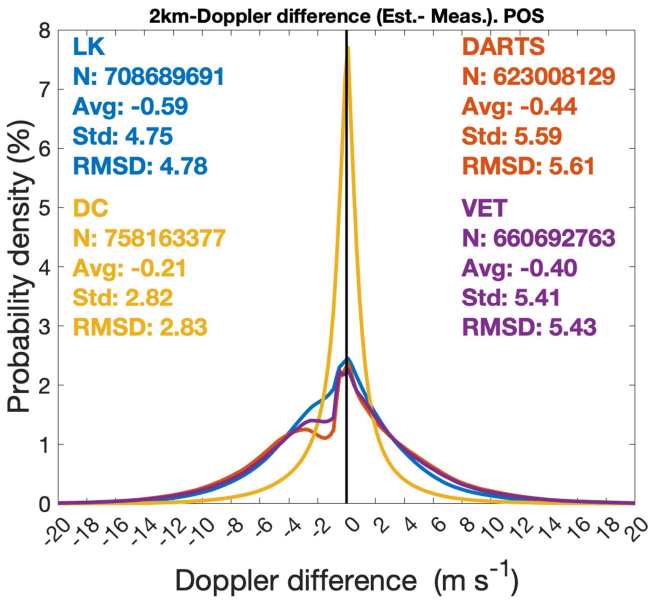

(b)

Fig. 8. Doppler difference (reconstructed Doppler from RMVs—measured Doppler) distribution obtained considering CAPPI 2 km data and LK, DARTS, VET, and DC RMV methods (panel a). In panel b, situations where reconstructed Doppler and the measured one have an opposite sign, are filtered out. In the panel's legend, *N*, Avg, Std, and RMSD indicate the number of samples, the average, and standard deviation difference and the RMSD, respectively.

8.5° and 20° in terms of 99th percentile and maximum value, respectively. This means that, the term $\sin(\theta_k)$ is lower than $\sin(8.5°)= 0.15$ in the 99% of cases. Consequently, in most of cases, W_h results reduced by more than 85% thus supporting our approximation of (9).

Thus, other two equations, in addition to (9), are necessary to solve the problem. This is typically obtained considering two additional independent observations of V_{Dk} at the same kth position. This allow to obtain $U_x(k)$, $U_y(k)$, and $W_h(k)$ for each k position where the intersection of the three radar observations occur. This is obliviously a strong drawback because typical coverage in radar networks do not show extended overlapping areas and then the resulting motion vector retrievals cannot cover the whole network domain. To overcome this limitation, the Doppler observations within a given analysis window can be considered to build a set of Doppler measurements sufficiently independent to each other (see Fig. 5). Hence, a cost function to be minimized (J_{DC}), that include the summation of the squared differences between reconstructed Doppler, V_{Dk} and the observed one (V_{Dk}^{obs}), is considered. The term J_{DC}, is built considering the $N_p = n \times n$ grid points belonging to an analysis window, which is centered in the visited (x, y) grid point. Something similar was proposed in [23], [24], and [25] in which:

1) a more elaborated analysis windows is chosen;
2) an interpolating procedure is performed within the cost function; and
3) at least two radar have to contribute to the Doppler in the analysis window selected

$$J_{\mathrm{DC}}(\mathbf{U}) = \sum_{k=1}^{N_p} (V_{Dk} - V_{Dk}^{\mathrm{obs}})^2. \tag{10}$$

The final solution is obtained by nullifying the partial deviates of (10), obtaining the following:

$$\mathbf{U}(x, y, t) = \mathbf{M}^{-1}\mathbf{c} \tag{11}$$

where the matrix $\mathbf{M}$ and $\mathbf{c}$ are as follows:

$$\mathbf{M}^{-1} = \frac{1}{\Delta}\begin{bmatrix} \sum_{k=1}^{N_p}(\cos^2\phi_k\cos^2\theta_k) & -\sum_{k=1}^{N_p}(\cos\phi_k\sin\phi_k\cos^2\theta_k) \\ -\sum_{k=1}^{N_p}(\cos\phi_k\sin\phi_k\cos^2\theta_k) & \sum_{k=1}^{N_p}(\sin^2\phi_k\cos^2\theta_k) \end{bmatrix} \tag{12}$$

$$\mathbf{c} = \begin{bmatrix} \sum_{k=1}^{N_p}(V_{Dk}^{\mathrm{obs}}\sin\phi_k cos\theta_k) \\ -\sum_{k=1}^{N_p}(V_{Dk}^{\mathrm{obs}}\cos\phi_k cos\theta_k) \end{bmatrix} \tag{13}$$

$$\Delta = \sum_{k=1}^{N_p}(\sin^2\phi_k\cos^2\theta_k)\sum_{k=1}^{N_p}(\cos^2\phi_k\cos^2\theta_k) + - \left(\sum_{k=1}^{N_p}\cos\phi_k\sin\phi_k\cos^2\theta_k\right)^2. \tag{14}$$

The estimation process described in (11)–(13) repeats, sliding the analysis windows across the couples of grid points (x, y) covering for the whole radar domain.

Note that to simplify calculations in (11)–(13), as in LK method, two out of three components, that is U_x and U_y, are considered. From (10), it is evident as the DC technique is able to retrieve horizontal motion vectors which are representative of $n \times n$ boxes and for this reason the method can some lack of resolution if the size, n, of the analysis window is too small. However, n cannot be selected too small, because sufficiently independent Doppler observations have to be guaranteed within

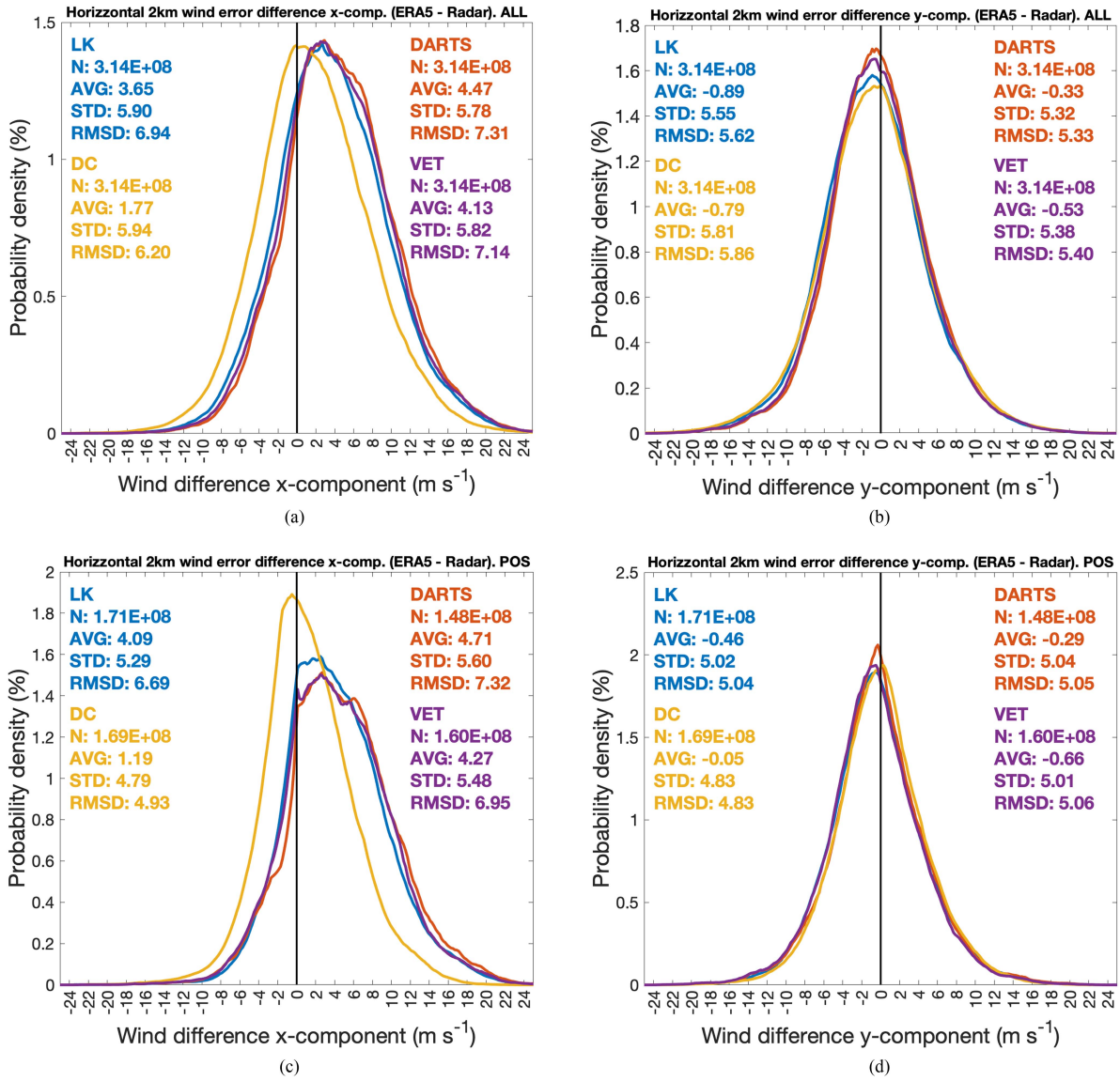

Fig. 9. Overall distribution of the difference between ERA5 wind and radar-retrieved RMV components in terms of zonal (left) and meridional (right) components. Upper panels are referred to the whole dataset, whereas the lower panels refer to cases where the deviation of the ERA5 wind directions from those of the RMV is within $\pm 90°$.

the analysis window to be able to invert the matrix $\mathbf{M}$. After some tests, n is fixed to 20 in this work. For smaller n, the resulting motion vectors are quite variable in space, while as n increases, the motion vectors get more and more spatially consistent. For $n \geq 20$, no sensible difference are noted in the estimated RMV in terms of motion directions, whereas the RMV peaks get progressively smoother. An example of the sensitivity for different choices of n is given later in the next section.

V. Results

In this section, quantitative results are presented. The quantitative characterization of the estimated RMV is not an easy task because, except for dedicated and limited field campaigns that involve aircraft flying through clouds, at the moment, there are no quantitative and direct information of in-cloud horizontal winds on national wide scales. Then, to characterize the errors in motion vector fields we used three independent approaches. The first one relies on the use of measured radar Doppler as reference, the second one considers ERA5 reanalysis as yardstick, while in the third one the classical precipitation nowcasting approach is implemented.

An illustrative example that may help the reader to have a qualitative idea of the RMV reconstructions using all the methods exposed in Section VI, is given in Fig. 6. From this figure (left) is clear as all the methods based on the solution of the optical flow equation show a small dynamic variation of the intensity of the RMV field. Contrarily, the DC method reveals a much higher intensity variations within the represented cyclone. Looking at the agreement of the estimated RMV with measured Doppler (right panels), it is glaringly obvious how the best agreement is found when Doppler data are used in the

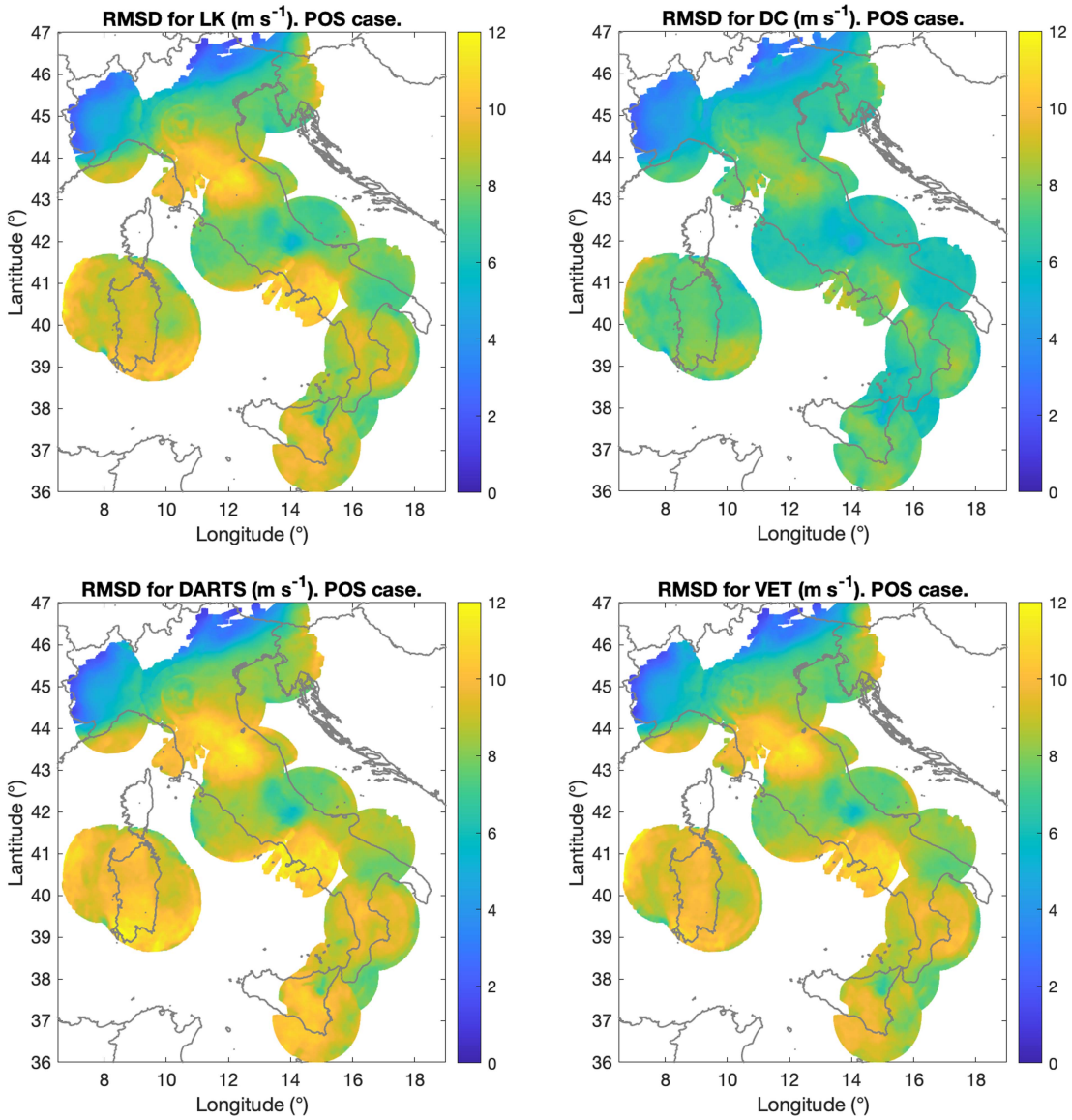

Fig. 10. Spatial distribution of the RMSD between ERA5 wind and radar-retrieved RMV components in the "POS" case of Fig. 9.

estimation process (i.e., for the DC method). However, it is more important to observe as DARTS, LK and VET suffer of lack of representatives of the intensity of RMVs, thus producing large errors when compared with measured Doppler. Fig. 7 shows the dependence of the DC RVM output quality as a function of the window size n for the same case study analyzed in Fig. 6. It is clear as the choice of n play a role in the agreement of the reconstructed RMV field with the measured Doppler (a)–(c). The optimum value for n is found to be equal to 20 [d] although it can oscillate on a case-by-case basis. However, larger n tends to guarantee a more robust spatial homogeneity of the final result and for this reason $n = 20$ is selected in this analysis.

A. Comparison of RMV With Doppler Measurements

The first comparison is accomplished taking the measured radar Doppler as reference. This is clearly unfair for DC method since it directly uses Doppler in the estimation process. So for DC, the Doppler-based comparison has the meaning to verify if the method was correctly implemented. Fig. 8(a) shows the Doppler Difference distribution (i.e., reconstructed Doppler from U_x and U_y from LK, DARTS, VET and DC minus measured Doppler) and the related error statistics for the implemented RMV methods. As expected, DC has a peak around the origin indicating the effectiveness of the minimization in (10). The other methods show a negative bias (underestimation) oscillating around –1 ms^{-1} with a root mean square error difference larger than 5.37 ms^{-1}. Things slightly improve if we remove gross errors (i.e., opposite directions of the measured with respect to reconstructed Doppler), as evidenced in Fig. 8(b).

B. Comparison of RMV With ERA5

To expand quantitative evaluation to the DC method more fairly, ERA5 wind components are taken as reference. In this case, a direct comparison of the zonal and meridional wind

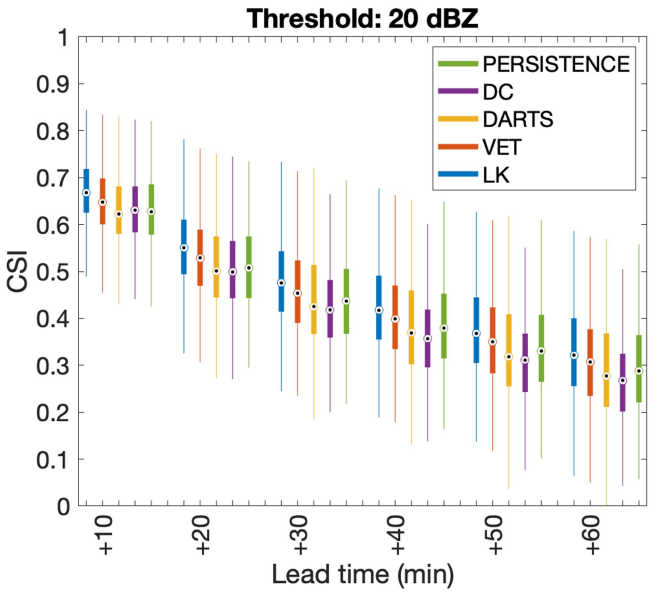

Fig. 11. Critical success index versus advection lead time for various RMVs, plus persistence case, as specified in the panel's legend. On each box, the central mark indicates the median, whereas the bottom and top edges of the box indicate the 25th and 75th percentiles, respectively. Thin lines extension represents the outliers domain.

component is performed. As done previously, radar data are averaged on the 31 km × 31 km window to homogenize the spatial resolution to that of ERA5. Then, a cubic interpolation is applied to project ERA5 wind components in the radar grid. The ERA5 minus radar RMVs distribution is shown in Fig. 9(a) and (b). DC RMV performs better than the other methods with an evident improvement in the East–West x-component. Most of the improvement is in the bias (1.77 ms^{-1} for DC) which is almost an half with respect the best performing method among LK, VET, and DARTS which tend to underestimate compared to ERA5. This result might be connected to what is shown in the example of Fig. 6, in which the DC RMV intensity is much larger than that output by the other methods. It is worth highlighting that ERA5 gives horizontal winds (i.e., movement of air masses), whereas radar-based motion vectors agree with movement of hydrometeors. Net of the intrinsic discrepancies in the different RMV methodologies used, the two quantities (i.e., air masses and hydrometor motion) have to converge at some point, as suggested by Fig. 9. Panels c) and d) of the same figure, replicate panels a) and b) but selecting only those component directions that agree to each other. As for the other kind of comparison, the difference between DC and the other RMV methods increases strengthening the fact that DC is in a better agreement with the general circulation represented by ERA5. To check the spatial distribution of the differences between ERA5 winds and radar RMV, Fig. 10 shows the root-mean-square difference (RMSD) obtained as the square root of the sum of the squared RMSD of the single meriodional and zonal components. RMSD is built taking the temporal sequence of ERA5 and RMV outputs at each grid point of the radar mosaic. These temporal sequences must have at least 100 valid samples to be considered in the final maps of Fig. 10. From this figure, the advantage of using DC is evident, whereas the other methods tend to have large discrepancies in the Middle North area, Sardinia (left island), and the southern part. This can be partially due to local effects caused by the orography and/or local circulation.

C. Comparison of RVMs Using a Precipitation Nowcasting Approach

The last way to compare RMV performances is within a precipitation nowcasting framework. The idea is to feed the same advection scheme with all the RMVs previously generated and test their performance in terms of the difference of the advected reflectivity field (Z_n) with the measured one (Z). In formulas, it is

$$Z_n(x, y, n\Delta t) = Z(x - U_x n\Delta t, y - U_y n\Delta t) \tag{15}$$

being $n\Delta t$ the lead time of the advection and U_x, U_y the tested motion fields from DC, DARTS, VET, and LK. The comparative analysis is dealt with in terms of the critical success score (CSI)

$$\mathrm{CSI(th)} = \frac{h}{h + m + f} \tag{16}$$

where h, m, and f are the hit (# samples for which $Z \geq$ th and $Z_n \geq$ th), miss (# samples for which $Z \geq$ th and $Z_n <$ th), false (# samples for which $Z <$ th and $Z_n \geq$ th) for a given threshold th. Fig. 11 shows the CSI for th=20 dBZ. Considering the large variability of CSI associated to each trial with the various RMV used, all of them seem to be practically equivalent to each other in terms of precipitation nowcasting evaluation approach. However, on average LK gives some advantage over the other estimation methods, while the DC (implemented with a window size $n = 20$) does not give any improvements (it even performs worst). Spatial gradients in the motion vector intensity from DC could be responsible of bad radar precipitation nowcasting performance because (15) works properly if the terms, U_x and U_y, are spatially homogeneous (i.e., slow varying). This is likely not happening for DC given its ability to better mimic the motion vector intensity variations than VET, DARTS, and LK. DC with a smaller window size, i.e., $n = 5$, is also tested, producing a deterioration in CSI performance of about –3% than for $n = 20$. A larger spatial variability of the DC motion vector is expected in this case, thus confirming the bad performance of radar pattern advection (15). Similar conclusions are obtained when considering the semilagrangian approach in Germann and Zawadzkiz's [19] work although test were performed on a case study basis. These results discourages the use of DC RMV retrieval in simple advection schemes, promoting its use mainly as a standalone product for climate records, ground reference for future satellite missions, and additional input in the definition of radar-based warning flags.

VI. Conclusion

In this work, one year and half of weather radar data from the Italian network are considered to extract the motion vector fields within precipitation clouds and quantitatively characterize their statistical error. Among the existing and more popular

approaches, namely LK, DARTS, and VET, a Doppler based one (DC) is proposed taking advantage of the findings from previous studies. To this end, a national wide mosaic of Doppler is generated which is, in our knowledge, an uncommon practice. The DC method successfully minimizes its output rain motion components with respect to the measured Doppler whereas the other methods fail in doing that especially in terms of enhanced error difference standard deviation which is larger than 5 ms^{-1} compared to nearly 4 ms^{-1} for DC. DC seems to outperform the other methods when compared with reanalysis fields ERA5 too. Although reanalysis and radar derived RMV represent different quantities at different spatial scales, their inter-comparison is acceptable with bias improvement, brought by DC, that can reach peaks of 50%. Unfortunately, when compared within a precipitation nowcasting framework, DC shows lower performances whereas LK results more suitable. Instead, the DC methodology should be preferred to generate products of more accurate RMV requested for many important applications, such as to aid future space borne validation programs, fed climate records at regional scale, and contribute to improve radar-based warning indexes. Future work could be devoted to developing a combined approach among the RMVs presented here to capture the best from each of them to find a better agreement with all the different metrics of comparison.

Appendix A
DC Methodology: Equations

The DC method requires the minimization of the cost function (J) to obtain an estimate of the zonal and meridional rain motion components, $U_x(l)$ and $U_y(l)$, respectively, at position lth, which is centered in a $N_p = n \times n$ moving analysis window [see Fig. 5]

$$J = \sum_{k=1}^{N_p} (V_{Dk} - V_{Dk}^{\mathrm{obs}})^2 \tag{17}$$

where V_{Dk}^{obs} is the observed Doppler at position kth, whereas V_{Dk} is the expected Doppler projection as a function of U_x and U_y

$$V_{Dk} = U_x \sin(\phi_k)\cos(\theta_k) + U_y \cos(\phi_k)\cos(\theta_k). \tag{18}$$

In the latter equation we discarded the vertical component for easy of calculations and we did not use the position index l to not overload the notation. Hence, using (18) into (17), taking the partial derivatives of J with respect to U_x and U_y and putting them to zero, we have

$$\frac{\partial J}{\partial U_x} = 0 \Rightarrow 2\sum_{k=1}^{N_p} (V_{Dk} - V_{Dk}^{\mathrm{obs}})\sin\phi_k\cos\theta_k \tag{19a}$$

$$\frac{\partial J}{\partial U_y} = 0 \Rightarrow 2\sum_{k=1}^{N_p} (V_{Dk} - V_{Dk}^{\mathrm{obs}})\cos\phi_k\cos\theta_k. \tag{19b}$$

Then using (18) into (19) we have

$$\sum_{k=1}^{N_p} (U_x \sin^2\phi_k\cos^2\theta_k + U_y \cos\phi_k\cos^2\theta_k\sin\phi_k - V_{Dk}^{\mathrm{obs}}\sin\phi_k\cos\theta_k) = 0 \tag{20a}$$

$$\sum_{k=1}^{N_p} (U_x \sin\phi_k\cos^2\theta_k\cos\phi_k + U_y \cos^2\phi_k\cos^2\theta_k - V_{Dk}^{\mathrm{obs}}\cos\phi_k\cos\theta_k) = 0. \tag{20b}$$

Because U_x and U_y uniquely depend by the position index l, which coincides with the center of the moving analysis window, those terms can be grouped outside the summation terms and consequently we can further write

$$U_x\left[\sum_{k=1}^{N_p} (\sin^2\phi_k\cos^2\theta_k)\right] + U_y\left[\sum_{k=1}^{N_p} (\cos\phi_k\cos^2\theta_k\sin\phi_k)\right] = \sum_{k=1}^{N_p} (V_{Dk}^{\mathrm{obs}}\sin\phi_k\cos\theta_k) \tag{21a}$$

$$U_x\left[\sum_{k=1}^{N_p} (\sin\phi_k\cos^2\theta_k\cos\phi_k)\right] + U_y\left[\sum_{k=1}^{N_p} (\cos^2\phi_k\cos^2\theta_k)\right] = \sum_{k=1}^{N_p} (V_{Dk}^{\mathrm{obs}}\cos\phi_k\cos\theta_k). \tag{21b}$$

The latter is a linear systems that can be written in a matrix form

$$\mathbf{MU} = \mathbf{c} \tag{22}$$

where $\mathbf{U(l)} = [U_x(l), Uy(l)]^T$ and

$$\mathbf{M} = \begin{bmatrix} \sum_{k=1}^{N_p} (\sin^2\phi_k\cos^2\theta_k) & \sum_{k=1}^{N_p} (\cos\phi_k\cos^2\theta_k\sin\phi_k) \\ \sum_{k=1}^{N_p} (\sin\phi_k\cos^2\theta_k\cos\phi_k) & \sum_{k=1}^{N_p} (\cos^2\phi_k\cos^2\theta_k) \end{bmatrix} \tag{23a}$$

$$\mathbf{c} = \begin{bmatrix} \sum_{k=1}^{N_p} (V_{Dk}^{\mathrm{obs}}\sin\phi_k\cos\theta_k) \\ \sum_{k=1}^{N_p} (V_{Dk}^{\mathrm{obs}}\cos\phi_k\cos\theta_k) \end{bmatrix}. \tag{23b}$$

Finally, the solution $\mathbf{U}$ is obtained inverting $\mathbf{M}$

$$\mathbf{U}(l) = \mathbf{M}^{-1}\mathbf{c} \tag{24}$$

with

$$\mathbf{M}^{-1} = \frac{1}{\Delta}\begin{bmatrix} \sum_{k=1}^{N_p} (\cos^2\phi_k\cos^2\theta_k) & -\sum_{k=1}^{N_p} (\cos\phi_k\sin\phi_k\cos^2\theta_k) \\ -\sum_{k=1}^{N_p} (\cos\phi_k\sin\phi_k\cos^2\theta_k) & \sum_{k=1}^{N_p} (\sin^2\phi_k\cos^2\theta_k) \end{bmatrix} \tag{25}$$

$$\Delta = \sum_{k=1}^{N_p} (\sin^2\phi_k\cos^2\theta_k)\sum_{k=1}^{N_p} (\cos^2\phi_k\cos^2\theta_k) + - \left(\sum_{k=1}^{N_p} \cos\phi_k\sin\phi_k\cos^2\theta_k\right)^2. \tag{26}$$

Equations (23b)–(26) are iterated across the positions lth and valid Doppler data to obtain the final RMV field.

ACKNOWLEDGMENT

The authors would like to thank the Civil Protection Department under the cooperative agreement 2022–2024.

REFERENCES

[1] A. G. Straume-Lindner and P. Ingmann, "ADM-Aeolus: The first space-based high spectral resolution Doppler Wind Lidar," in *Proc. IEEE Int. Geosci. Remote Sens. Symp.*, 2007, pp. 4969–4974.
[2] M. Rennie and L. Isaksen, "The NWP impact of Aeolus level-2B winds at ECMWF, 06/2020," 2020.
[3] P. Kiriakidis et al., "The impact of using assimilated aeolus wind data on regional WRF-chem dust simulations," *Atmospheric Chem. Phys.*, vol. 23, no. 7, pp. 4391–4417, 2023.
[4] C. Feng and Z. Pu, "The impacts of assimilating aeolus horizontal line-of-sight winds on numerical predictions of hurricane IDA (2021) and a mesoscale convective system over the atlantic ocean," *Atmospheric Meas. Techn.*, vol. 16, no. 10, pp. 2691–2708, 2023.
[5] T. Fujita, "Present status of cloud velocity computations from ATS-1 and ATS-3," *Space Res.*, vol. 9, pp. 557–570, 1968.
[6] S. J. Nieman et al., "Fully automated cloud-drift winds in NESDIS operations," *Bull. Amer. Meteorological Soc.*, vol. 78, pp. 1121–1134, 1997.
[7] D. Santek et al., "2019 Atmospheric motion vector (AMV) intercomparison study," *Remote Sens.*, vol. 11, no. 19, 2019.
[8] J. S. Goerss, "Impact of satellite observations on the tropical cyclone track forecasts of the navy operational global atmospheric prediction system," *Monthly Weather Rev.*, vol. 137, pp. 41–50, 2009.
[9] C. S. Velden, W. E. Lewis, W. Bresky, D. Stettner, J. Daniels, and S. Wanzong, "Assimilation of high-resolution satellite-derived atmospheric motion vectors: Impact on HWRF forecasts of tropical cyclone track and intensity," *Mon. Wea. Rev.*, vol. 145, pp. 1107–1125, 2017.
[10] J. Vogelzang and A. Stoffelen, "Scatterometer wind vector products for application in meteorology and oceanography," *J. Sea Res.*, vol. 74, pp. 16–25, 2012, Special Issue on Physics of Sea and Ocean.
[11] A. J. Illingworth et al., "The EarthCARE satellite: The next step forward in global measurements of clouds, aerosols, precipitation, and radiation," *Bull. Amer. Meteorological Soc.*, vol. 96, no. 8, pp. 1311–1332, 2015.
[12] S. Prasanth et al., "Quantifying the vertical transport in convective storms using time sequences of radar reflectivity observations," *J. Geophysical Res.: Atmos.*, vol. 128, no. 10, 2023, Art. no. e2022JD037701.
[13] A. J. Illingworth et al., "WIVERN: A new satellite concept to provide global in-cloud winds, precipitation, and cloud properties," *Bull. Amer. Meteorological Soc.*, vol. 99, no. 8, pp. 1669–1687, 2018.
[14] R. Rinehart and E. Garvey, "Three-dimensional storm motion detection by conventional weather radar," *Nature*, vol. 273, pp. 287–289, 1978.
[15] V. Poli, P. Alberoni, and D. Cesari, "Intercomparison of two nowcasting methods: Preliminary analysis," *Meteorological Atmos. Phys.*, vol. 101, pp. 229–244, 2008.
[16] M. Montopoli, F. S. Marzano, E. Picciotti, and G. Vulpiani, "Spatially-adaptive advection radar technique for precipitation mosaic nowcasting," *IEEE J. Sel. Topics Appl. Earth Observ. Remote Sens.*, vol. 5, no. 3, pp. 874–884, Jun. 2012.
[17] L. Li, W. Schmid, and J. Joss, "Nowcasting of motion and growth of precipitation with radar over a complex orography," *J. Appl. Meteorol. Climatol.*, vol. 34, no. 6, pp. 1286–1300, 1995.
[18] S. Laroche and I. Zawadzki, "Retrievals of horizontal winds from single-doppler clear-air data by methods of cross correlation and variational analysis," *J. Atmospheric Ocean. Technol.*, vol. 12, no. 4, pp. 721–738, 1995.
[19] U. Germann and I. Zawadzki, "Scale-dependence of the predictability of precipitation from continental radar images. Part I: Description of the methodology," *Monthly Weather Rev.*, vol. 130, no. 12, pp. 2859–2873, 2002.
[20] E. Ruzanski and V. Chandrasekar, "Scale filtering for improved nowcasting performance in a high-resolution X-band radar network," *IEEE TGRS*, vol. 49, no. 6, pp. 2296–2307, Jun. 2011.
[21] D. B. Lucas and T. Kanadec, "An iterative image registration technique with an application to stereo vision," in *Proc. Eur. Conf. Comput. Vis.*, 1981, pp. 674–679.
[22] S. Song, B. Beh, and R. K. Moore, "Scan patterns and accuracy of a radar wind sensor (RAWS)," Tech. Rep., 1995.
[23] O. Bousquet and M. Chong, "A multiple-Doppler synthesis and continuity adjustment technique (MUSCAT) to recover wind components from Doppler radar measurements," *J. Atmospheric Ocean. Technol.*, vol. 15, no. 2, pp. 343–359, 1998.
[24] O. Bousquet and P. Tabary, "Development of a nationwide real-time 3-D wind and reflectivity radar composite in France," *Quart. J. Roy. Meteorological Soc.*, vol. 140, no. 679, pp. 611–625, 2014.
[25] C. Xue, Z. Ding, X. Shen, and X. Chen, "Three-dimensional wind field retrieved from dual-doppler radar based on a variational method: Refinement of vertical velocity estimates," *Adv. Atmospheric Sci.*, vol. 39, pp. 145–160, 2022.
[26] H. Hersbach et al., "The era5 global reanalysis," *Quart. J. Roy. Meteorological Soc.*, vol. 146, no. 730, pp. 1999–2049, 2020.
[27] M. Taszarek, N. Pilguj, J. T. Allen, V. Gensini, H. E. Brooks, and P. Szuster, "Comparison of convective parameters derived from era5 and merra-2 with rawinsonde data over Europe and north America," *J. Climate*, vol. 34, no. 8, pp. 3211–3237, 2021.
[28] J. Huang et al., "Evaluation of five reanalysis products with radiosonde observations over the central Taklimakan desert during summer," *Earth Space Sci.*, vol. 8, no. 5, 2021, Art. no. e2021EA001707.
[29] R. Bonanno, M. Lacavalla, and S. Sperati, "A. new high-resolution meteorological reanalysis Italian dataset: MERIDA," *Quart. J. Roy. Meteorological Soc.*, vol. 145, no. 721, pp. 1756–1779, 2019.
[30] S. Schimanke et al., "Copernicus European regional reanalysis," *Proc. EMS Annu. Meeting*, vol. 18, p. 389, 2021.
[31] A. Rinollo et al., "Definition and impact of a quality index for radar-based reference measurements in the H-SAF precipitation product validation," *Nat. Hazards Earth Syst. Sci.*, vol. 13, pp. 2695–2705, 2013.
[32] S. Pulkkinen et al., "Pysteps: An open-source python library for probabilistic precipitation nowcasting (v1.0)," *Geoscientific Model Develop.*, vol. 12, no. 10, pp. 4185–4219, 2019.
[33] I. M. Navon and D. M. Legler, "Conjugate-gradient methods for large-scale minimization in meteorology," *Monthly Weather Rev.*, vol. 115, no. 8, pp. 1479–1502, 1987.
[34] S. Laroche and I. Zawadzki, "A variational analysis method for retrieval of three-dimensional wind field from single-doppler radar data," *J. Atmospheric Sci.*, vol. 51, no. 18, pp. 2664–2682, 1994.
[35] M. R. Rauber and S. W. Nesbitt, *Radar Meteorology: A. First Course*. New York, NY, USA: Wiley, Apr. 2018.

Mario Montopoli received the Laurea degree in electronic engineering from the University of L' Aquila, L' Aquila, Italy, in 2004, and the Ph.D. degree in methods and technologies for environmental monitoring from the University of Basilicata, Potenza, Italy, in 2008.

He is a Permanent Senior Researcher with the Institute of Atmospheric Sciences and Climate (ISAC), National Research Council of Italy (CNR), Rome, Italy. He has more than ten-year experience with Earth observation techniques, including studies to improve retrieval algorithms of: 1) liquid/solid precipitation-related quantities using microwave radars; 2) mass loading of ash as seen from active and passive microwave observations of volcanic emissions; and 3) radio propagations parameters of path attenuation using radiative transfer routines. In 2005, he was a Research Scientist of ground-based radar meteorology and microwave remote sensing with the Center of Excellence CETEMPS, L'Aquila. In 2006, he was a Research Assistant with the Department of Electrical Engineering and Information, University of L' Aquila. From 2011 to 2013, he was a Researcher with the Department of Geography, University of Cambridge, Cambridge, U.K., under the Marie Curie FP7 European Program. From 2014 to 2015, he was with the Department of Information Engineering, Sapienza University of Rome, Rome, Italy, and an EUMETSAT Visiting Scientist with the H-SAF Facility, Darmstadt, Germany.

Dr. Montopoli is an Associate Editor for IEEE GEOSCIENCE AND REMOTE SENSING LETTERS edited by the Institute of Electrical and Electronics Engineers (IEEE) since 2014. From Sept. 2021, he is a Member of the mission advisory group of the WIVERN mission, which is part of the European Space Agency Earth Explorer 11 ideas.

Clizia Annella received the bachelor's and master's degrees in mathematics from University of Siena, Siena, Italy, in 2013 and 2016, respectively.

She is currently a Research Assistant with the Center of Excellence Telesensing of Environment and Model Prediction of Severe events (CETEMPS), L'Aquila, Italy. Her research interests include precipitation nowcasting techniques based on deep learning approaches applied to weather radar data.

Luca Baldini (Senior Member, IEEE) received the Laurea degree in electrical engineering and the Ph.D. degree in methods and technologies for environmental monitoring from the University of Florence, Florence, Italy, in 1988 and 1994, respectively.

From 1994 and 2001, he was a Lecturer with the University of Siena, Siena, Italy, teaching remote sensing systems, and with the University of Florence, teaching signal theory, in 1996. Concurrently, from 1995 to 2001, he was an independent consultant. In 2001, he joined the Institute of Atmospheric Sciences and Climate of the National Research Council of Italy (CNR-ISAC), Rome, Italy, where he supervises research on precipitation measurements, with a particular focus on radar polarimetry applied to quantitative precipitation estimation for hydrological applications and the characterization of precipitation microphysics. From 2003 to 2004, he was a Visiting Scholar with Colorado State University, Fort Collins, CO, USA, and with the University of Helsinki, Helsinki, Finland, in 2010. Since 2009, he has been a part of the NASA PMM (Precipitation Measuring Missions) science team. He participated in the LPVEx and CHUVA campaigns in preparation for the NASA/JAXA Global Precipitation Measuring mission. In 2012, he coordinated NASA's contribution to the experimental activities in Italy as part of the HyMeX experiment.

Dr. Baldini has been a Member of the ESA Mission Advisory Group for the ESA/JAXA EarthCARE mission since May 2017.

Elisa Adirosi received the master's degree in environmental engineering and the Ph.D. degree in environmental and hydraulic engineering from the Sapienza University of Rome, Rome, Italy, in 2009 and 2015, respectively.

She has been a Visiting Scientist with Goddard Space Flight Center, NASA, Greenbelt, MD, USA, and a Researcher with the Institute of Atmospheric Sciences and Climate, National Research Council (CNR-ISAC), Rome, Italy. She has more than ten years of experience in analyzing precipitation data and investigates the characteristics of simulated and observed drop size distributions to improve precipitation retrieval from remote sensing measurements.She has been involved in several national and international projects on this topic.

Vincenzo Capozzi was born in Avellino, Italy, in 1986. He received the master's degree (*magna cum laude*) in climate science from the University of Naples, Naples, Italy, in 2012, where he received the Ph.D. degree.

In 2016, he defended his Ph.D. thesis titled "X-band weather radar measurements: raingauge-based adjustment and meteorological applications." In the same year, he received a Professional Certification (in compliance with the recommendations of World Meteorological Organization) as Meteorologist. In 2017, he was a Postdoctoral Researcher with the Department of Science and Technology, University of Naples. Since 2017, he been also working as Broadcast Meteorologist with RAI – RadiotelevisioneItaliana. His research interests include radar meteorology, experimental meteorology, reconstruction of past climate in the Mediterranean area, and synoptic climatology.

Dr. Capozzi was an Assistant Professor of synoptic meteorology and analysis of weather conditions with the University of Naples, from 2022.

Gianfranco Vulpiani received the Laurea degree in physics and the Ph.D. degree in radar meteorology from the University of L'Aquila, L'Aquila, Italy, in 2001 and 2005, respectively.

From 2001 to 2005, he was with the CETEMPS Center of Excellence, University of L'Aquila. In 2004, he was a Visiting Scholar with the Department of Electrical Engineering, Colorado State University, Fort Collins, CO, USA, working on the development of artificial intelligence techniques for radar data processing. In 2006, he was Postdoctoral Researcher with the Observing Systems Department, Météo France, Paris, France, in the context of the European project FLYSAFE project, focusing his research activities on hail precipitation characterization. Since 2007, he has been a Senior Scientific Officer with the National Department of Civil Protection, dealing with the analysis and management of natural hazards in the framework of the national Early Warning System. His research interests include the development of radar data processing techniques, quantitative precipitation estimation, microphysics of meteorological and volcanic ash clouds, simulation and analysis of electromagnetic scattering processes. In this context, he coordinates the technical and scientific activities related to the management and development of the national radar network.

Dr. Vulpiani has been an Associate Editor for the journal *Atmospheric Measurement Techniques* of the European Geosciences Union since 2014.